Biphasic concentration patterns in ionic transport under nanoconfinement revealed in steady state and time-dependent properties

María Queralt-Martín[1] Jose J. Pérez-Grau[1,2], Laidy M. Alvero González[1], D. Aurora Perini[1], Javier Cervera[3], Vicente M. Aguilella[1] and Antonio Alcaraz[1]*

[1]Laboratory of Molecular Biophysics, Department of Physics, Universitat Jaume I, E-12071 Castellón, Spain

[2]Departament de Física Aplicada, Universitat Politécnica de València, E-46022 València, Spain

[3]Departament de Física de la Terra i Termodinàmica, Universitat de València, E-46100 Burjassot, Spain.

Abstract

Ion permeation across nanoscopic structures differs considerably from microfluidics because of strong steric constraints, transformed solvent properties and charge-regulation effects revealed mostly in diluted solutions. However, little is known about nanofluidics in moderately concentrated solutions, which are critically important for industrial applications and living systems. Here we show that nanoconfinement triggers general biphasic concentration patterns in a myriad of ion transport properties using two contrasting systems: a biological ion channel and a much larger synthetic nanopore. Our findings show a low concentration regime ruled by classical Debye screening and another one where ion-ion correlations and enhanced ion-surface interactions contribute differently to each electrophysiological property. Thus, different quantities (e.g., conductance vs noise) measured under the same conditions may appear contradictory because they belong to different concentration regimes. In addition, non-linear effects that are barely visible in bulk conductivity only in extremely concentrated solutions become apparent in nanochannels around physiological conditions.

Keywords

Ion Channel | Synthetic nanopore | nanofluidics | Ion transport | single-molecule electrophysiology | Nanoscale confinement | Concentrated solutions

1. Introduction

The transport of ions in membrane systems is a field of intense research in physical chemistry and particularly in bio- and electrochemistry [1–4]. However, nature is not scale-invariant: as the size of objects decreases, dominant effects may become negligible and vice versa[5]. Therefore, nanofluidics is not a direct extension of microfluidics towards smaller scales[6], but involves unexpected behaviors like dielectric saturation of confined water[7,8], rectified ion transport[9], electroneutrality breakdown[10,11] and overlapping electric double layers[12,13] among many others[14]. Remarkably, most of these findings involve dilute solutions that have received preferential attention for several reasons. On the one side, solutions with low ion density are considered ideal, which simplifies their thermodynamic description, as shown in the seminal work of Debye, Hückel and Onsager (DHO) [2,15] with regard to ionic conductivity. On the other side, dilute solutions are of

capital importance in industrial recovery processes [16] and in mimicking physiologically relevant conditions (ionic strength in living cells and in human blood plasma is approximately ~ 0.15 M) [17,18].

However, moderately concentrated solutions have become increasingly interesting for electrochemical reactors[19–21], water desalination[22] and bioelectrochemistry[23]. Indeed, particular technological applications such as supercapacitors, rechargeable batteries and energy-storage devices require extremely concentrated solutions. From a theoretical point of view, concentrated solutions require more elaborate approaches than the DHO theory: incorporating effects like dielectric friction during the movement of ions, ion advection by the fluid or hard-core repulsion between ions [15,24,25]. Although refined models provide remarkable agreement with experiments for some strong electrolytes [15], and empirical models are available that simultaneously correlate conductivity, concentration and temperature for mixed solutions and weak electrolytes [25], some properties of concentrated solutions remain poorly understood. For instance, the decrease in screening length with increasing concentration characteristic of the Debye theory is not found experimentally in concentrated solutions, but a transition to a new regime appears where the screening length increases with concentration [17].

Here, we aim to take a broader perspective and investigate the impact of concentrated solutions on ion permeation through nanochannels. To do so, we measured conductance and ionic selectivity, performed noise analysis (current fluctuations and gating) and thermodynamic analysis (activation energy E_a) in a biological ion channel and a synthetic nanopore for a wide range of electrolyte concentrations. We specifically selected two systems with divergent properties, the bacterial porin OmpF [26–29] and the polyimide conical nanopore (PI NP) [30,31]. Considering OmpF versus PI NP, neither the geometrical shape (hourglass versus conical) nor the pore diameter (~1-4 nm versus 30-200 nm) or the pore length (~5 nm versus ~10 μm) are comparable as shown in Figure 1A. There are also differences in the charge distribution, as OmpF has a highly heterogeneous distribution of charged residues causing a strong transversal electrostatic field at the central narrowing [29,32], whereas the PI conical nanopore is more homogeneously charged with carboxylic acid groups [33]. Furthermore, OmpF channel displays ohmic conduction at neutral pH [34] whereas PI NP shows diode-like current rectification under the same conditions [35] (Figure S1A).

Despite their dissimilarities, both in OmpF and in PI NP we find biphasic concentration patterns in all studied quantities. These results reveal two separate concentration regimes regulating ion transport: one in dilute solutions compatible with classical Debye screening as described by DHO theory, and the other in concentrated solutions where the concentration pattern is inverted. We critically discuss the origin of this latter trend, finding that several factors (ionic diffusion, ion-ion and ion-pore interactions among others) may contribute differently to each measured quantity. In summary, the correspondence between our experimental results obtained in dissimilar systems points to the universality of the reported biphasic patterns, while the mechanisms behind may be system- and quantity-dependent.

2. Experimental

2.1 Biological ion channel OmpF

OmpF channel measurements were carried out by reconstituting a single OmpF protein into a planar lipid membrane formed by using the solvent free modified Montal-Muller technique [36,37]. Briefly, lipid was prepared by dissolving diphytanoylphosphatidylcholine (DPhPC) (Avanti polar lipids, Inc., Alabaster, AL) in pentane (Baker) after chloroform evaporation. Aliquots of 10–20 μL of 5 mg/mL DPhPC were added on top of each salt solution in two 1.8 mL compartments (so-called *cis* and *trans*) of a Teflon chamber. The two compartments were separated by a 15 μm-thick Teflon film with a 70–100 μm diameter orifice where the membrane is formed. The orifice was pre-treated with a 3% solution of hexadecane in pentane. After pentane evaporation, the level of solutions in each compartment was raised above the hole so the planar bilayer could form by apposition of the two monolayers. Channel reconstitution was achieved by adding 0.1 μL of OmpF protein at 1 ng/mL in 1 M KCl and 1% (v/v) OctylPOE (Alexis, Switzerland) to one side of the membrane. OmpF was a kind gift of Dr. S. M. Bezrukov (NIH, Bethesda, MD, USA).

2.2 Polyimide conical synthetic nanopore

The polyimide nanopore (PI NP) used in our experiments was fabricated by foil irradiation with heavy ions as explained previously[30,31]. Subsequently, the ion tracks were converted into nanopores by exposing the polymer membrane to chemical etching with a strong inorganic etchant under asymmetric conditions. The membrane was placed in an electrochemical cell separating two salt solutions. The solution pH was in the range 6.5–7.0 during measurements. Because these pH values are higher than the pKa characteristic of the −COOH moieties functionalized on the pore surface, the carboxylic acid groups were ionized to $-COO^-$ and thus the pore was negatively charged. The resulting nanopore has an approximate conical shape (so called bullet-like). The radius of the pore base was obtained by direct imaging of the region, while pore tip radius was estimated from the nanopore electrical conductance, obtaining ~100 nm (base) and ~15 nm (tip).

2.3 Electrical measurements

The chamber for OmpF or PI NP electrical measurements was connected to an Axopatch 200B amplifier (Molecular Devices, Sunnyvale, CA) in the voltage-clamp mode through Ag/AgCl electrodes covered with 2 M KCl, 1.5 % agarose bridges assembled within standard 250 μL pipette tips. The working electrode was placed in the *cis* side, whereas the *trans* side was set to ground. Thus, the potential is defined as positive when it is higher on the *cis* side. In OmpF measurements, *cis* was the side of protein addition while in PI NP experiments, the nanopore was placed so that its tip (narrow opening) faced the *cis* side. Data from the amplifier were filtered by an integrated low pass 8-pole Bessel filter at 10 kHz, digitized with a Digidata 1440A (Molecular Devices, Sunnyvale, CA) at a sampling frequency of 50 kHz and analyzed using pClamp 10.7 software (Molecular Devices, Sunnyvale, CA). The chamber and the head stage were isolated from external noise sources with a double metal screen (Amuneal Manufacturing Corp., Philadelphia, PA). The described set-up can measure currents of the order of picoamperes or above with a time resolution below the millisecond.
Electrolyte (monovalent or divalent) solutions were adjusted at pH 6 and controlled during the experiments using a GLP22 pH meter (Crison). To assure reproducibility, the bacterial porin OmpF experiments were repeated a minimum of 3 times. Also, the whole measurements of conductance in PI NP were completed in the same day, to avoid NP instabilities.

2.4 Conductance Measurements

Nanopore conductance (defined as G = I/V) was obtained from current recordings in symmetric electrolyte solutions at +100 mV (OmpF) and +1 V (PI NP). Current values were obtained from current traces using the Gaussian fit tool of Clampfit 10.7 (Molecular Devices, Sunnyvale, CA). Generally, the OmpF channel shows ohmic current-voltage (I-V) curves, whereas PI NP displays current rectification (see Figure S1A).

2.5 Current fluctuation analysis

The power spectral density (PSD) of current fluctuations was obtained directly from the measured current traces with the pClamp 10.7 software (Molecular Devices, LLC.) by calculating the Fast Fourier Transform from the digitized signal (Figure S1B). The power spectrum generates a frequency domain representation of the time domain data, revealing the power levels of different frequency components in the signal. The PSD spectral resolution used was 0.76 Hz and, for each signal, the available spectral segments were averaged. Then, PSD values at each applied potential were averaged in the 1–10 Hz band. These data ($<S_I>$) were plotted as a function of the measured current (Figure S1C) to obtain the so-called parabolic coefficient S_G/G^2 from fitting the equation $<S_I> = (S_G/G^2)I^2$. Note that in the case of PI NP, noise analysis is limited to V > 0 because for V < 0 the system shows limiting current involving non-equilibrium features [38,39].

2.6 Ion selectivity measurements

Selectivity was assessed by measuring the reversal potential (RP), which is the applied voltage needed to null the current measured when a salt concentration gradient is imposed in the system. If the pore is neutral, RP equals zero, while it becomes nonzero when the channel is selective to anions or cations. All RP values were corrected by the liquid junction potential calculated using Henderson's equation to eliminate the contribution of the electrode KCl-agarose bridges [40].

2.7 Thermodynamic analysis

The activation energy (E_a) was obtained from the Arrhenius equation

$$G = A \cdot \exp\left(-\frac{E_a}{RT}\right)$$

as the slope of the corresponding Arrhenius plot (ln G vs 1/T). These experiments were carried out with the chamber attached to a recirculating water box connected to a thermostatic bath. Temperature was changed from room temperature (22.0 ± 0.1 °C) to 42.0 ± 0.1 °C. Channel conductance was measured when the system reached thermal equilibrium. The temperature in the chamber was controlled with a probe connected to a multimeter (Promax Instruments).

3. Results and Discussion

3.1 Biphasic Concentration Patterns

First, we measured the solution conductivity of KCl up to 4 M and LiCl up to 12 M, as shown in Figure 1B. LiCl was used in addition to KCl because of its much higher solubility that allows the extension of the study to higher concentrations. As predicted by DHO theory, KCl and LiCl conductivities scale almost linearly with concentration in dilute solutions (actually $\kappa \sim c^{0.8}$) albeit minor (KCl) and substantial (LiCl) deviations from this trend are visible in molar concentrations. Clearly, some effects such as long-range ion-ion correlations and solvent excluded-volume, ignored in the DHO approach, become important in concentrated solutions [15,41].

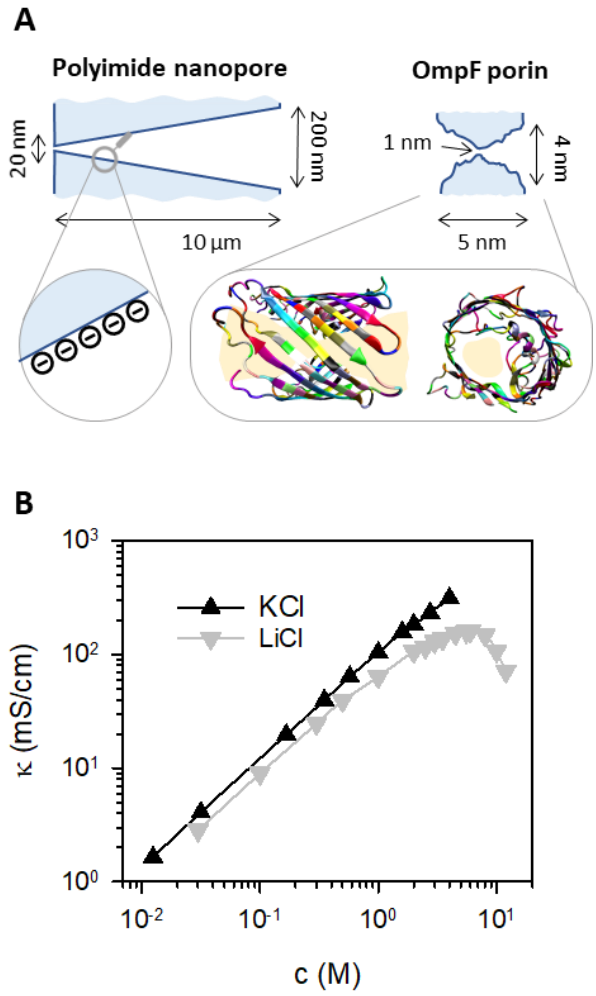

Figure 1.- (A) Schematic representation of the OmpF porin and the PI nanopore. Cartoon is not to scale. Insets represent the presence of negatively charged carboxyl groups in the nanopore wall and the actual protein structure (side and front views) of OmpF. Yellow areas in the structure represent the zone available for ion and water transport. **(B)** Measured electrical conductivity as a function of solution concentration for KCl and LiCl.

Figure 2 shows the concentration dependence of four different quantities measured in the biological channel OmpF (left) and the PI conical nanopore (right) (see Figure S2A for a direct comparison of all data series). Figure 2A displays the single-channel conductance of OmpF and PI NP obtained from current-voltage relationships (see Figure S1A) with some interesting features becoming apparent. Regarding the importance of the pore dimensions, note that the actual slope in the G-c relationships is larger in OmpF than in PI NP (see Figure S2A) because of the contribution of access resistance [42–44] that is dominant in the narrow and short biological channel whereas it is minor (if any) in the wide and long synthetic nanopore. In contrast, G experiments in LiCl for OmpF and PI NP share the fact that the monotonic trends in G are broken with maxima around c ~ 5 M, clearly below the maximum present in κ measurements in LiCl at higher concentrations (c ~ 6 M) (see Figure S3A for a direct comparison between normalized solution conductivity and channel conductance). The shift of the maxima in G-c curves in relation to κ-c curves suggests that nanoscale confinement present in conductance measurements may boost the effects responsible of the nonlinear pattern found in bulk conductivity.

Although we only present biphasic concentration patterns in G experiments of monovalent salts using LiCl, nonlinear G-c curves have also been reported in other electrolytes and systems. For instance, cylindrical nanopores of different dimensions and materials show biphasic patterns in KCl, NaCl and LiCl [45,46], which are linked to short-time current blockages originated from counterions transiently adsorbed at the pore surface [46]. In addition, non-linear G-c relationships of biological channels appear in gramidicin A in KCl and CsCl [43,47], and in the narrow and highly occupied potassium channels where this behavior was connected to ion-ion repulsion and steric constrains [48].

Figure 2B presents the dependence of the current excess noise on concentration using the parabolic coefficient S_G/G^2, which contains relevant kinetic physicochemical information of the intrinsic system fluctuations not directly visible in G measurements [49–51]. The power spectral density (PSD) is calculated via the Fourier transform of the recorded current versus time at different applied voltages (Figure S1B), finding a parabolic scaling in the low frequency band $\langle S_I \rangle \sim I^2$ characteristic of equilibrium fluctuations [51] (Figure S1C). S_G/G^2 is obtained using the equation $\langle S_I \rangle = (S_G/G^2)I^2$ for each concentration, as shown in Figure 2B. Interestingly, S_G/G^2 shows biphasic concentration patterns for both KCl and LiCl in the two nanochannels, with variable inflection points for each system at salt concentrations of c ~ 1-2 M. The low concentration region of all experiments is compatible with surface charge fluctuations [50] where G changes with c as shown in Figure 2A, while S_G is constant. This suggests that in diluted solutions the number of surface-bound fluctuating particles does not change with increasing concentration, probably because of electroneutrality requirements. However, in the high concentration regime S_G/G^2 increases rapidly with c (only glimpsed in PI NP in KCl) implying that S_G should increase with concentration as happens in the occurrence of binding processes [49] also described as ion trapping at the pore surface [52]. Remarkably, the high-concentration regime is clearly visible in noise experiments for both KCl and LiCl at moderate concentrations, whereas in G measurements it is only discernible in LiCl and at much higher concentrations than in the corresponding power spectral density measurements. This indicates that the transition between low- and high-concentration regimes is not universal, but depends on the quantity under study.

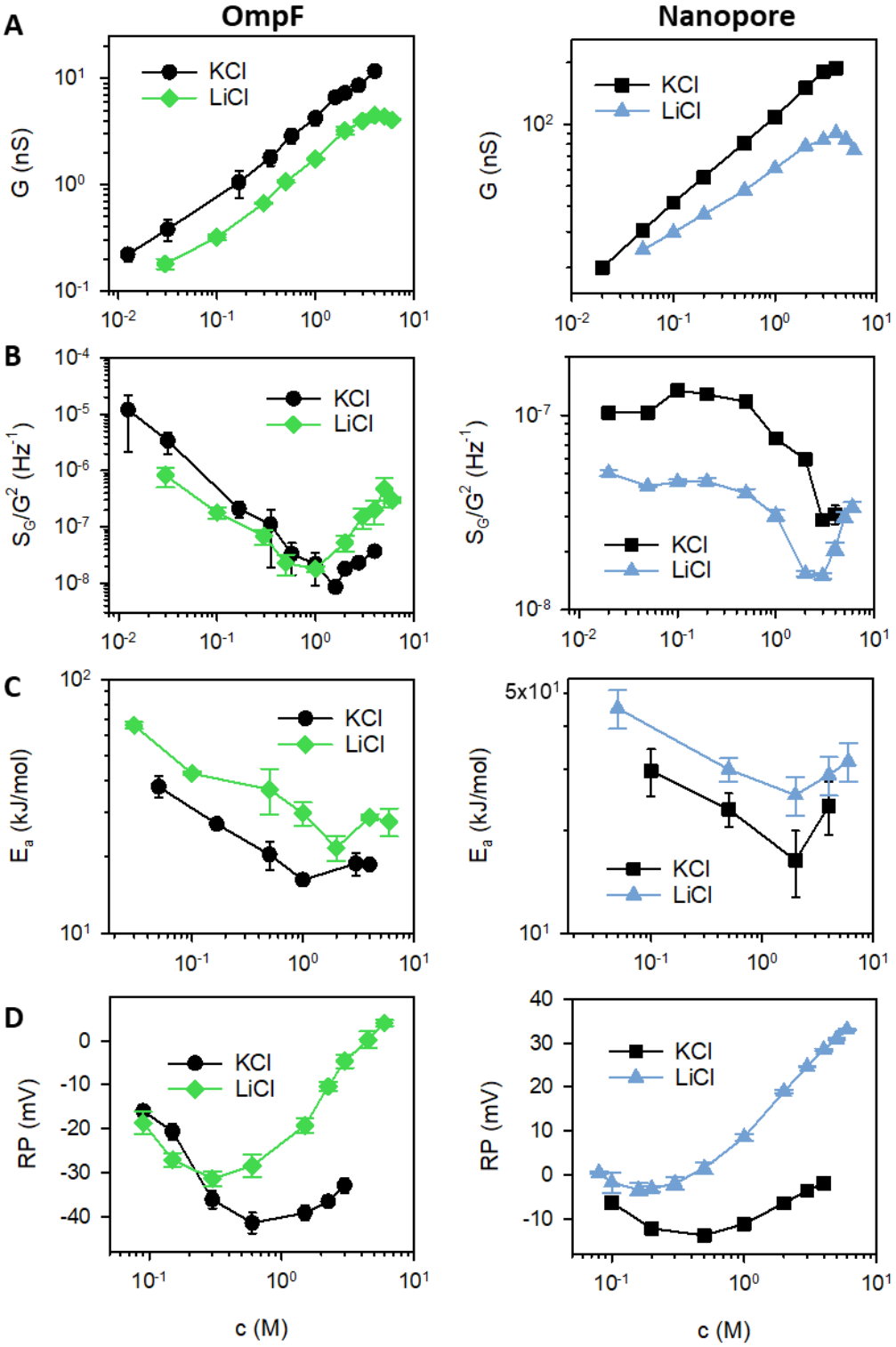

Figure 2.- Biphasic concentration scaling under nano-confinement. Measured single channel conductance G **(A)**, excess noise S_G/G^2 **(B)**, activation energy E_a **(C)**, and reversal potential RP **(D)** of OmpF porin (left) and a PI conical nanopore (right) as a function of solution concentration for KCl and LiCl at pH 6. In A, the conductance was

measured at +100 mV for OmpF and +1 V for the PI conical nanopore. In B, the parabolic coefficient S_G/G^2 was calculated from the excess noise in the range -100 mV to +100 mV for OmpF and 0 V to +1 V for the nanopore. In C, the activation energy was calculated from conductance measurements in the temperature range 10-35 °C. In D, RP was measured using a fixed salt concentration in the *trans* side (0.03 M for OmpF and 0.05 M for PI NP) while varying the concentration on the *cis* side. The horizontal axis corresponds to *cis* side concentration, which was always higher than that of the *trans* side.

Figure 2C shows the concentration scaling of a thermodynamic property, the activation energy E_a. Each value of E_a plotted in Figure 2C was calculated by performing an Arrhenius plot from KCl or LiCl conductance measurements in the temperature range 20-40°C (Figure S1D). Notably, OmpF-conductance activation energy E_a considerably exceeds that of the bathing solution conductivity (Figure S2C), in agreement with recent studies on the mitochondrial channel VDAC [53]. Like G and S_G/G^2 data, the activation energy barriers show two different trends with concentration, with inflection points around 1- 2 M. Similar biphasic patterns were found in E_a in the ionic conduction through silica nanochannels [54] and also in the Li^+ transfer across interfaces between solid electrodes and electrolyte solutions [55]. Remarkably, these results were linked to different mechanisms, namely specific ion adsorption at the pore surface in the case of silica nanochannels [56] and the solvation structure of concentrated Li^+ solutions in the vicinity of the electrode interface differing from that in bulk solution [55].

We next investigated whether the reported non-monotonic trends are also present in quasi-equilibrium selectivity experiments involving a transmembrane concentration gradient. The voltage required to yield zero current when ions flow downhill, the so-called reversal potential (RP) in the ion channel literature [57] or membrane potential in ion-exchange membranes [4 3], provides an estimation of the pore preference for anions or cations. Figure 2D shows RP measurements of OmpF (left) and PI NP (right) in different concentration gradients of KCl and LiCl as a function of the highest concentration (*cis* side). Increasing concentrations in the *cis* side lead to non-monotonic trends for RP. Similar patterns have been reported for a number of different biological and abiotic membrane systems such as the mitochondrial channel VDAC [58], other synthetic nanopores [59,60] and ion exchange membranes [61]. Of note, detailed theoretical studies agree in ascribing the initial increase of absolute RP with concentration gradient to electrostatic exclusion, while the subsequent decrease at higher concentration is linked to the diffusional contribution that dominates in this regime [62 63]. Moreover, there is coincidence in pointing out that, in order to reproduce the experimental non-monotonic trends, either in RP or in the membrane potential, the counterion diffusion coefficient must be reduced with respect to that of the co-ion, pointing to an attractive interaction between the counterion and the membrane fixed charges [3,61,64–66]. Finally, note that experiments at high concentrations of LiCl lead to positive values of RP that for $c_{cis} > c_{trans}$ imply anion-selective pores[62] showing selectivity inversion. This result is very significant in the context of charge inversion with monovalent ions [67], an effect that cannot be described using the strongly correlated liquid theory[68].

Another property often considered to characterize the response of biological channels to changes in membrane polarization, a key cellular and intracellular mechanism, is the voltage-induced gating. It refers to conformational transitions between fully conductive

(open) states and other (closed) states where transport of ions or other metabolites is partially or totally inhibited [69]. Although PI NP does not show voltage-induced closures and a direct comparison is not possible, it is noteworthy that in OmpF porin, voltage gating also exhibits a biphasic scaling with concentration (Figure S4). In contrast to conductance data that are steady state measurements, gating experiments account for an explicitly time-dependent property that can be quantified as the lifetime τ of the open channel. Although the relationship between channel open conductance and its lifetime is not evident, similar biphasic concentration patterns for G and τ have been reported in the channels formed by the antibiotic peptide gramicidin A [70]. In addition, biphasic concentration dependences have been recently reported by studies on the kinetics of α-cyclodextrin interaction with the ΔCymA channel [71].

3.2 Comparison Between Reduced Biphasic Properties

The use of reduced properties in both axes allows to see if experiments that look quite different could actually correspond to the same relative pattern. The solution conductivity κ is a paradigmatic example of that: different salts show biphasic concentration patterns that differ significantly from each other in the values of κ_{max} and c_{max} (the concentration of the peak κ_{max}) (see Figure S5A for the case of LiCl and $MgCl_2$). However, when experiments are plotted in reduced form, all curves overlap as shown in Figure S5B (see normalization procedure in the caption of Figure S5B). Interestingly, an exhaustive study including salts of monovalent and multivalent cations [72] shows overlapping patterns for reduced κ-c curves ascribing the universality of the relative decrease at high concentration to the fact that ion crowding is so high that are not enough solvent molecules to achieve bulk-like ion solvation.

Keeping in mind normalized κ-c relationships, we use reduced quantities in G, S_G/G^2, and E_a that show biphasic concentration patterns in KCl and LiCl (see normalization procedure in the caption of Figure 3) . Figure 3A shows G/G_{max} versus c/c_{max} for OmpF and PI in KCl and LiCl. Interestingly, not all curves come together but there is a better agreement between reduced G-c curves when grouped by nanochannel (i.e. KCl and LiCl in OmpF) than when grouped by electrolyte (i.e. KCl in OmpF and PI NP). We interpret these findings considering that G is an integral quantity that gathers contributions from the overall system in terms of pore dimensions and shape, residue chemistry and particular solute confinement. Accordingly, experiments in KCl and LiCl in OmpF (or in PI NP) yield similar reduced conductance whereas experiments in the same electrolyte performed in OmpF and in PI NP differ from each other.

Quite in contrast, reduced noise coefficient S_G/G^2-c curves (Figure 3B) are better grouped together by electrolyte (i.e. LiCl for OmpF and PI NP) than by system (i.e. KCl and LiCl in PI NP). Because time-dependent properties are usually non additive but depend on a critical rate-determining step [73], and considering that S_G/G^2 in OmpF is ruled by surface-governed fluctuations [49], we hypothesize that in this case the particular cation chemistry is the ruling factor and not the pore dimensions or the channel charges. In fact, normalized experimental results in another time-dependent phenomenon like OmpF gating follow the same trend as S_G/G^2 because reduced τ-c curves with KCl and LiCl do not overlap but differ significantly (Figure S6).

Interestingly, reduced E_a-c curves shown in Figure 3C present a different situation because data series can be grouped neither by system nor by electrolyte despite the ubiquity of the general biphasic trend. Each experiment seems to present a singular combination of energetic barriers that depend on system geometry (interfacial access resistance) and the ion-specificity characteristic of adsorption processes.

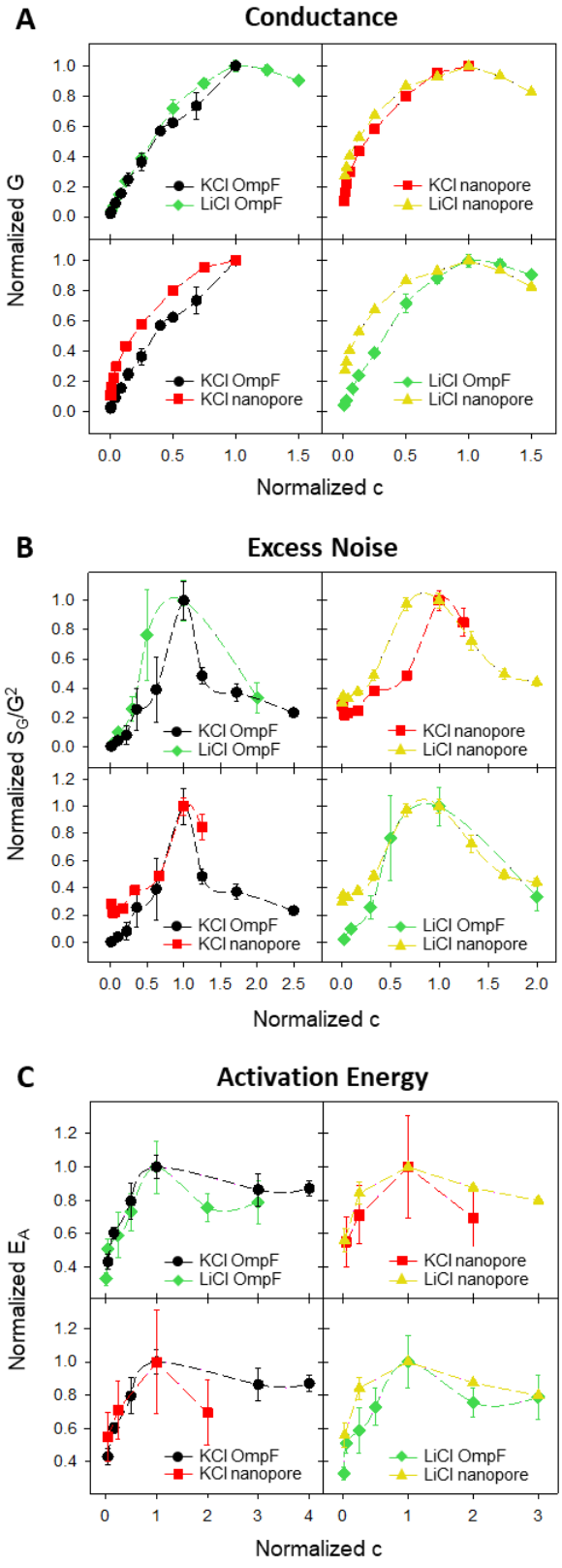

Figure 3.- Normalized concentration scaling of various ion transport properties is grouped by system or by ion. Normalized conductance (A), excess noise (B), and activation energy (C) as a function of normalized concentration measured in OmpF or the PI nanopore, in KCl and LiCl salt solutions. Here and elsewhere, normalizations were performed by dividing each value of G, S_G/G^2 or E_A by the maximum in the corresponding series, G/G_{max}, $(S_G/G^2)/(S_G/G^2)_{max}$ or E_A/E_{Amax}. Then, concentration was normalized independently for each series by dividing c by the concentration of the corresponding maximum value, $c(G_{max})$, $c((S_G/G^2)_{max})$, or $c(E_{Amax})$.

3.3 Interaction of Nanochannels With Divalent Cations

Next, we performed complementary experiments in $MgCl_2$, a salt that in the case of OmpF has been proved to reverse the intrinsic cationic selectivity of the channel into anionic one [40,74] due to the binding of Mg^{2+} ions in the central narrow constriction of the channel. Similar findings have been reported in synthetic nanopores [75,76] and particularly in PI nanopores [35,63].

Figure S3B shows the reduced conductivity κ/κ_{max} in $MgCl_2$ and the corresponding reduced conductance G/G_{max} measured both in OmpF and PI NP. Comparison between reduced κ and G evidences that in $MgCl_2$ solutions G_{max} is reached at lower concentrations than κ_{max} and this shifting is considerably larger than in measurements with LiCl (Figure S3A). Of note, measurements in $MgCl_2$ in Figure S3B show that G_{max} in PI NP appears at a lower concentration than in OmpF, in contrast to measurements in LiCl where G_{max} was found at the same c for both channels.

To investigate $MgCl_2$-pore interactions, we compare reduced properties in the divalent salt with those obtained in monovalent salts, as shown in Figure 4. Figure 4A shows G/G_{max} versus c/c_{max} in OmpF and PI NP in KCl, LiCl and $MgCl_2$. In OmpF we see that plots for divalent cations and monovalent ones overlap, emphasizing that G in this channel is regulated by structural factors and not by cation-pore specific interactions [40]. On the contrary, measurements in PI NP show that $MgCl_2$ induces a visible change in the position of the maximum of the G-c curve towards lower concentrations (also visible in Figure S3B) than LiCl and KCl. We conclude that the interaction of Mg^{2+} with PI COO^- groups is much more intense than with OmpF residues. Reduced noise measurements in Figure 4B also show that Mg^{2+} interaction is slightly different in each channel (OmpF and PI NP), what emphasizes the importance of the particular magnesium-pore chemistry.

RP measurements in salts of $MgCl_2$ show also biphasic patterns in OmpF and PI NP (Figure 5A) but, unfortunately, these experiments do not allow the use of reduced quantities because both positive and negative values are attained, so that any attempt of normalization distorts the overall shape of the curve. In view of that, we considered that RP reflects the addition of electrostatic exclusion and ionic diffusion [62]. Accordingly, exclusion effects dominate for low concentration gradients where noticeable differences are found between OmpF and NP PI, in line with findings shown in Figure 4. However, when we focus on large concentration gradients, where diffusional effects prevail, we can observe how the slope of the curve in the logarithmic scale (actually proportional to Planck's diffusion potential) is better grouped by ion than by system (Figure 5B). This is to say, different RP experiments in OmpF show diverse slopes, but

these are very similar in $MgCl_2$ experiments with OmpF and NP PI (same reasoning for LiCl and KCl). The fact that the "effective" diffusional contribution could be so similar in such contrasting systems (similarly to noise experiments in Figure 3 and Figure 4) points to ion-ion interactions as the major ruling factor as opposed to ion-pore interactions.

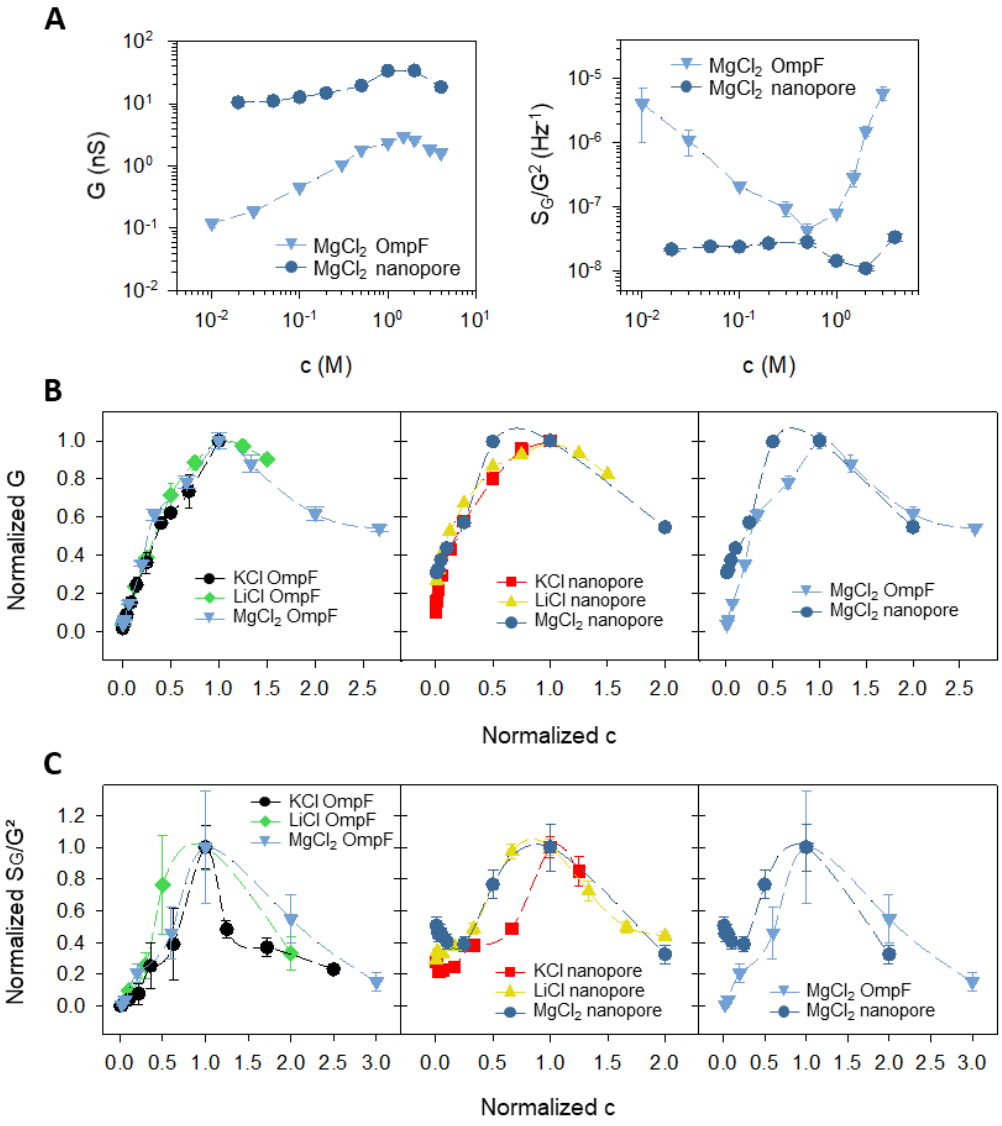

Figure 4.- The biphasic pattern is reproduced in $MgCl_2$. (A) Measured single channel conductance G (*left*) and excess noise S_G/G^2 (*right*) as a function of solution concentration for OmpF and PI conical nanopore. Conductance was measured at +100 mV for OmpF and +1 V for the PI conical nanopore. The parabolic coefficient S_G/G^2 was calculated from the excess noise in the range -100 mV to +100 mV for OmpF and 0 to +1 V for the nanopore. **(B-C)** Reduced properties in OmpF and PI nanopore as a function of reduced concentration measured in KCl, LiCl and $MgCl_2$ salt solutions. (B) Normalized conductance. (C) Normalized excess noise. The two quantities represented in the vertical axes are

normalized with respect to the corresponding peak values in each plot, as in Figure 3.

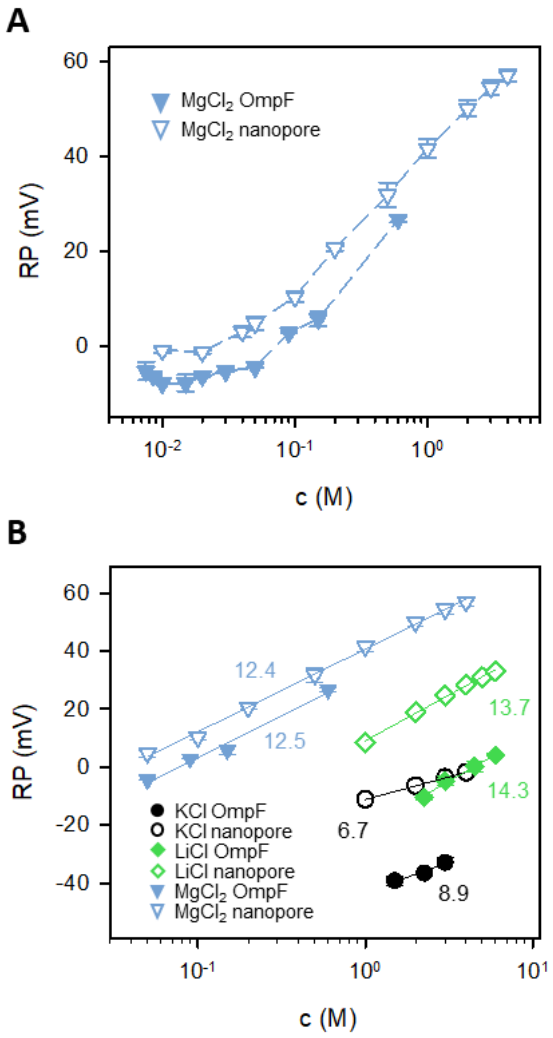

Figure 5.- Slopes of reversal potential (RP) measurements are grouped by ion. **(A)** Reversal potential (RP) as a function of solution concentration in the *cis* side, measured in $MgCl_2$. Data were obtained with a concentration in the *trans* side of 5 mM. **(B)** RP measurements vs salt concentration in the *cis* side measured for OmpF and PI NP in KCl, LiCl or $MgCl_2$ salts. Solid lines are logarithmic fits $y = a\,lnx + b$, with the slope *a* indicated next to each fit. Concentration in the *trans* side was 30 mM (KCl OmpF, LiCl OmpF), 50 mM (KCl PI NP, LiCl PI NP), or 5 mM ($MgCl_2$ OmpF, $MgCl_2$ PI NP).

3.4 On the mechanisms Behind Biphasic Patterns

Customarily, ion permeation through membrane channels has been described as a combination of electrostatic exclusion, ionic diffusion and adsorption processes to the pore sites [40,57,77]. Such a conceptual framework can explain why ionic fluxes saturate with increasing concentration in particular systems [57], but fails to account for generalized biphasic patterns in such contrasting systems as the ones shown here.

In previous sections, we have mentioned several mechanisms that could be behind the observed biphasic concentration patterns. On the one side, it is known that increasing salt concentrations lower the permittivity of bulk solutions due to the disruption of solvent structure in the vicinity of the ions [78 79]. Also, it has been reported that nanoscale confinement decreases the translational and rotational mobility of water molecules due to locally high electric fields and low-permittivity membrane interfaces [7,80,81]. Accordingly, we hypothesize that the shifting towards lower concentrations of the inflection point in G-c, S_G/G^2-c, E_a-c, RP-c and τ-c relationships (Figure 2 and S4) with respect to κ-c (Figure 1B) is in part related to the different dielectric properties of confined water with respect to bulk one, the latter being more efficient than the former to screen coulombic interactions between charged ions [79]. On the other side, multiple effects not directly related to the solvent but involving the pore structural features and charge distribution (visible in G and E_a experiments), specific pore-ion chemistry (experiments with $MgCl_2$) and the intrinsic properties of the salt ions (RP, gating and noise experiments) must be invoked to explain the evident differences behind biphasic patterns shown in Figures 2-5.

From our findings we cannot envision a unique mechanism ruling over the others, even it is unclear if a particular mechanism operates always in the same direction. Thus, recent studies focused on ion correlations show that positive correlations between ions moving in the same direction (as happens in RP experiments) are essentially different from anticorrelations when they move in opposite directions (G experiments)[82]. Besides, it has been reported that some operating mechanisms may not be independent but may act together synergistically. For instance, at high concentration the steric repulsion by excluded volume of ions could play an important role in reducing ion occupancy inside the channel, weakening ion-pore interactions [83]. Also, recent computational studies show the crucial role of ion−ion correlations in changing the intrinsic channel energetic barriers to ion permeation [84]. Likewise, adsorption of counterions onto the pore wall occurring at high concentration has been reported to change the pore net charge and also hinder the counterion effective mobility [3,49,57,62,85].

4. Conclusions

We find biphasic concentration patterns in steady-state or time-dependent voltage-driven experiments (G, S_G/G^2, and E_a) and also in quasi-equilibrium experiments with net zero-current (RP) both in the biological channel OmpF and PI synthetic conical nanopores. These parallel findings in contrasting nanoscale systems, together with scattered data available in the literature, show that bimodal concentration patterns existing in bulk solutions are altered and shifted towards lower concentrations in nanometer-sized membrane pores. Our results using diverse salts of monovalent and divalent cations suggest that several separate factors are behind the experimental findings.

We show that, in agreement with previous findings concerning the screening length [17], there are two separate concentration regimes regulating ion transport both in steady state and time-dependent experiments, one satisfactorily described by Debye screening in dilute solutions and another in concentrated solutions where a combination of factors leads to biphasic patterns. We conclude that the transition between both regimes is shifted under nanoconfinement towards less concentrated solutions (around physiological conditions) in comparison to bulk conductivity where it happens only in extreme conditions. Also, the inflection point occurs at different concentration in every type of measurement (current, noise, temperature, voltage-induced gating, selectivity) because each experimentally available property (G, S_G/G^2, E_a, RP and/or τ_0) arises from a particular balance between solvent properties, electrostatic exclusion, ionic diffusion, ion-ion and ion-pore interactions, being all these factors boosted by the nanoscale confinement.

A direct corollary of our study is that the concentration at which a given property will be incompatible with the classical Debye screening cannot be predicted from any other experiment where a different property is measured. This means that the widespread use of solution conductivity κ to discriminate between low- and high- concentration regimes could be particularly ill-suited to understand ion transport through nanochannels because all the consequences of nanoscale confinement are intrinsically absent in κ. In fact, even the nanopore conductance G could be ineffective to discriminate high-concentration effects that are clearly visible in other properties (S_G/G^2, E_a, RP and/or τ_0) as revealed in experiments with KCl.

Finally, note that our study contains thought-provoking implications for time-dependent experiments such as noise analysis and gating (customarily performed at high concentration to improve the signal to noise ratio), because their results in concentrated solutions could correspond to a non-Debye regime as opposed to conductance and selectivity experiments, usually performed at low salt concentration to get physiologically relevant information.

Supplementary Material

See the supplementary material for characteristic examples of different experiments, details of normalization procedures and additional data.

Conflicts of interest

There are no conflicts to declare

Acknowledgements

Authors acknowledge financial support by the Spanish Government MCIN/AEI/ 10.13039/501100011033 (Project 2019-108434GB-I00 to A.A., project IJC2018-035283-I to M.Q.M.), Universitat Jaume I (Project UJI-B2022-42 to A.A. and UJI-A2020-21 to M.Q.M and D.A.P), Generalitat Valenciana (Project GRISOLIAP/2018/061 to D.A.P. and A.A. and project AICO/2020/066 to A.A.).

References

[1] R. Robinson and R. Stokes, *Electrolyte Solutions* (Dover Publications, 2002).

[2] J. Bockris and A. Reddy, *Modern Electrochemistry 1* (Kluwer Academic Publishers, Boston, 1998).

[3] F. Helfferich, *Ion Exchange* (McGraw-Hill, New York, 1962).

[4] N. Laksminarayanaiah, *Transport Phenomena in Membranes* (Academic Press, New York, 1969).

[5] M. Wautelet, *Scaling Laws in the Macro-, Micro-and Nanoworlds* (2001).

[6] N. Kavokine, R.R. Netz, and L. Bocquet, Annu. Rev. Fluid Mech. **53**, 377 (2021).

[7] M. Aguilella-Arzo, A. Andrio, V.M. Aguilella, and A. Alcaraz, Phys. Chem. Chem. Phys. **11**, 358 (2009).

[8] L. Fumagalli, A. Esfandiar, R. Fabregas, S. Hu, P. Ares, A. Janardanan, Q. Yang, B. Radha, T. Taniguchi, K. Watanabe, G. Gomila, K.S. Novoselov, and A.K. Geim, Science (80-.). **360**, 1339 (2018).

[9] Z. Siwy and A. Fuliński, Am. J. Phys. **72**, 567 (2004).

[10] Z.X. Luo, Y.Z. Xing, Y.C. Ling, A. Kleinhammes, and Y. Wu, Nat. Commun. **6**, (2015).

[11] A. Levy, J.P. de Souza, and M.Z. Bazant, J. Colloid Interface Sci. **579**, 162 (2020).

[12] C. Duan and A. Majumdar, Nat. Nanotechnol. **5**, 848 (2010).

[13] Y. Green, J. Chem. Phys. **154**, (2021).

[14] L. Bocquet, Nat. Mater. **19**, 254 (2020).

[15] Y. Avni, R.M. Adar, D. Andelman, and H. Orland, Phys. Rev. Lett. **128**, 98002 (2022).

[16] L. Brückner, J. Frank, and T. Elwert, Metals (Basel). **10**, 1107 (2020).

[17] A.M. Smith, A.A. Lee, and S. Perkin, J. Phys. Chem. Lett. **7**, 2157 (2016).

[18] B. Liu, B. Poolman, and A.J. Boersma, ACS Chem. Biol. **12**, 2510 (2017).

[19] S.C. Perry, C. Ponce de León, and F.C. Walsh, J. Electrochem. Soc. **167**, 155525 (2020).

[20] T. Vidakovic-Koch, I. Gonzalez Martinez, R. Kuwertz, U. Kunz, T. Turek, and K. Sundmacher, Membranes (Basel). **2**, 510 (2012).

[21] R. Gao, S. Mosquera-Romero, E. Ntagia, X. Wang, K. Rabaey, and L. Bonin, J. Electrochem. Soc. **169**, 033505 (2022).

[22] B.A. Sharkh, A.A. Al-Amoudi, M. Farooque, C.M. Fellows, S. Ihm, S. Lee, S. Li, and N. Voutchkov, Npj Clean Water **5**, 9 (2022).

[23] D. Pletcher, in *Bioelectrochemistry* (John Wiley & Sons, Ltd, Chichester, UK, n.d.), pp. 327–358.

[24] J.-F.F. Dufrêche, O. Bernard, S. Durand-Vidal, and P. Turq, J. Phys. Chem. B **109**, 9873 (2005).

[25] W. Zhang, X. Chen, Y. Wang, L. Wu, and Y. Hu, ACS Omega **5**, 22465 (2020).

[26] S. Cowan, R. Garavito, J. Jansonius, J. Jenkins, R. Karlsson, N. König, E. Pai, R.

Pauptit, P. Rizkallah, J. Rosenbusch, G. Rummel, and T. Schirmer, Structure **3**, 1041 (1995).

[27] A.H. Delcour, Front. Biosci. **8**, 1132 (2003).

[28] H. Nikaido, Microbiol. Mol. Biol. Rev. **67**, 593 (2003).

[29] A. Alcaraz, E.M. Nestorovich, M. Aguilella-Arzo, V.M. Aguilella, and S.M. Bezrukov, Biophys. J. **87**, 943 (2004).

[30] Z. Siwy, D. Dobrev, R. Neumann, C. Trautmann, and K. Voss, Appl. Phys. A Mater. Sci. Process. **76**, 781 (2003).

[31] M. Ali, B. Schiedt, K. Healy, R. Neumann, and W. Ensinger, Nanotechnology **19**, 085713 (2008).

[32] S. Varma and E. Jakobsson, Biophys. J. **86**, 690 (2004).

[33] J. Cervera, B. Schiedt, R. Neumann, S. Mafá, and P. Ramírez, J. Chem. Phys. **124**, (2006).

[34] A. Alcaraz, P. Ramírez, E. García-Giménez, M.L. López, A. Andrio, and V.M. Aguilella, J. Phys. Chem. B **110**, 21205 (2006).

[35] P. Ramirez, J.A. Manzanares, J. Cervera, V. Gomez, M. Ali, S. Nasir, W. Ensinger, and S. Mafe, Electrochim. Acta **325**, 134914 (2019).

[36] S.M. Bezrukov and I. Vodyanoy, Biophys. J. **64**, 16 (1993).

[37] M. Montal and P. Mueller, Proc. Natl. Acad. Sci. U. S. A. **69**, 3561 (1972).

[38] M.R. Powell, I. Vlassiouk, C. Martens, and Z.S. Siwy, Phys. Rev. Lett. **103**, (2009).

[39] M. Queralt-Martín, D.A. Perini, and A. Alcaraz, Phys. Chem. Chem. Phys. **23**, 1352 (2021).

[40] A. Alcaraz, E.M. Nestorovich, M.L. López, E. García-Giménez, S.M. Bezrukov, and V.M. Aguilella, Biophys. J. **96**, 56 (2009).

[41] R.M. Adar, T. Markovich, A. Levy, H. Orland, and D. Andelman, J. Chem. Phys. **149**, 054504 (2018).

[42] E. Secchi, A. Niguès, L. Jubin, A. Siria, and L. Bocquet, Phys. Rev. Lett. **116**, (2016).

[43] M. Queralt-Martín, M.L. López, M. Aguilella-Arzo, V.M. Aguilella, and A. Alcaraz, Nano Lett. **18**, 6604 (2018).

[44] A. Alcaraz, M.L. López, M. Queralt-Martín, and V.M. Aguilella, ACS Nano **11**, 10392 (2017).

[45] H. Amiri, K.L. Shepard, C. Nuckolls, and R. Hernández Sánchez, Nano Lett. **17**, 1204 (2017).

[46] R. Tao, X. Gao, D. Lin, Y. Chen, Y. Jin, X. Chen, S. Yao, P. Huang, J. Zhang, and Z. Li, Phys. Fluids **33**, 012015 (2021).

[47] T.K. Rostovtseva, V.M. Aguilella, I. Vodyanoy, S.M. Bezrukov, and V.A. Parsegian, Biophys. J. **75**, 1783 (1998).

[48] B. Hille and W. Schwarz, J. Gen. Physiol. **72**, 409 (1978).

[49] M. Queralt-Martín, M.L. López, and A. Alcaraz, Phys. Rev. E - Stat. Nonlinear, Soft

Matter Phys. **91**, (2015).

[50] D.P. Hoogerheide, S. Garaj, and J.A. Golovchenko, Phys. Rev. Lett. **102**, (2009).

[51] S.M. Bezrukov and M. Winterhalter, Phys. Rev. Lett. **85**, 202 (2000).

[52] S. Su, X. Guo, Y. Fu, Y. Xie, X. Wang, and J. Xue, Nanoscale **12**, 8975 (2020).

[53] M. Queralt-Martín, D.P. Hoogerheide, S.Y. Noskov, A.M. Berezhkovskii, T.K. Rostovtseva, and S.M. Bezrukov, Biophys. J. **119**, 2584 (2020).

[54] C.L. Ritt, J.P. de Souza, M.G. Barsukov, S. Yosinski, M.Z. Bazant, M.A. Reed, and M. Elimelech, ACS Nano (2022).

[55] T. Doi, H. Oae, and M. Inaba, Electrochem. Sci. Adv. 1 (2021).

[56] C.L. Ritt, J.P. de Souza, M.G. Barsukov, S. Yosinski, M.Z. Bazant, M.A. Reed, and M. Elimelech, ACS Nano (2022).

[57] B. Hille, *Ion Channels of Excitable Membranes*, Third Ed. (Sinauer Associates Inc, Sunderland, MA, MA, 2001).

[58] E.B. Zambrowicz and M. Colombini, Biophys. J. **65**, 1093 (1993).

[59] W. Guo, L. Cao, J. Xia, F.Q. Nie, M. Wen, J. Xue, Y. Song, D. Zhu, Y. Wang, and L. Jiang, Adv. Funct. Mater. **20**, 1339 (2010).

[60] M. Nishizawa, V.P. Menon, and C.R. Martin, Science (80-.). **268**, 700 (1995).

[61] A.H. Galama, J.W. Post, H.V.M. Hamelers, V. V. Nikonenko, and P.M. Biesheuvel, J. Membr. Sci. Res. **2**, 128 (2016).

[62] M.L. López, M. Aguilella-Arzo, V.M. Aguilella, and A. Alcaraz, J. Phys. Chem. B **113**, 8745 (2009).

[63] P. Ramirez, J. Cervera, V. Gomez, M. Ali, S. Nasir, W. Ensinger, and S. Mafe, J. Memb. Sci. **573**, 579 (2019).

[64] P. Ramírez, S. Mafé, V.M. Aguilella, and A. Alcaraz, Phys. Rev. E. Stat. Nonlin. Soft Matter Phys. **68**, 11910 (2003).

[65] P. Ramírez, M. Aguilella-Arzo, A. Alcaraz, J. Cervera, and V.M. Aguilella, Cell Biochem. Biophys. **44**, 287 (2006).

[66] P. Ramírez, S. Mafé, A. Alcaraz, and J. Cervera, J. Phys. Chem. B **107**, 13178 (2003).

[67] M. Lidón López, M. Queralt-Martín, and A. Alcaraz, Electrochem. Commun. **48**, 32 (2014).

[68] W.S. Russell, C.-Y. Lin, and Z.S. Siwy, ACS Appl. Nano Mater. **5**, 17682 (2022).

[69] D.A. Perini, A. Alcaraz, and M. Queralt-Martín, Int. J. Mol. Sci. **20**, (2019).

[70] A. Ring and J. Sandblom, Biophys. J. **53**, 549 (1988).

[71] J.D. Prajapati, S. Pangeni, M.A. Aksoyoglu, M. Winterhalter, and U. Kleinekathöfer, ACS Nano **16**, 7701 (2022).

[72] V. V. Shcherbakov, Y.M. Artemkina, I.A. Akimova, and I.M. Artemkina, Materials (Basel). **14**, 5617 (2021).

[73] H.X. Zhou and A. Szabo, Biophys. J. **71**, 2440 (1996).

[74] E. García-Giménez, A. Alcaraz, and V.M. Aguilella, Phys. Rev. E - Stat. Nonlinear, Soft Matter Phys. **81**, (2010).

[75] Z.S. Siwy, M.R. Powell, A. Petrov, E. Kalman, C. Trautmann, and R.S. Eisenberg, Nano Lett. **6**, 1729 (2006).

[76] Z.S. Siwy, M.R. Powell, E. Kalman, R.D. Astumian, and R.S. Eisenberg, Nano Lett. **6**, 473 (2006).

[77] I. Santamaría-Holek, Z.J. Grzywna, and J.M. Rubi, Eur. Phys. J. Spec. Top. **222**, 129 (2013).

[78] W.R. Fawcett and A.C. Tikanen, J. Phys. Chem. **100**, 4251 (1996).

[79] T.R. Underwood and I.C. Bourg, J. Phys. Chem. B **126**, 2688 (2022).

[80] R.L. Fulton, J. Chem. Phys. **130**, (2009).

[81] K. Lebedev, S. Mafé, A. Alcaraz, and P. Ramírez, Chem. Phys. Lett. **326**, 87 (2000).

[82] N.M. Vargas-Barbosa and B. Roling, ChemElectroChem **7**, 367 (2020).

[83] D. Boda, W. Nonner, M. Valiskó, D. Henderson, B. Eisenberg, and D. Gillespie, Biophys. J. **93**, 1960 (2007).

[84] J.C. Ahumada, C. Alemán, J. Soto-Delgado, and J. Torras, J. Phys. Chem. B **123**, 86 (2019).

[85] B. Nadler, Z. Schuss, U. Hollerbach, and R.S. Eisenberg, Phys. Rev. E **70**, 051912 (2004).